



# Studies of Structural, Microstructure, Dielectric and Optical Properties of Bismuth-Based Complex Perovskite Modified Bismuth Ferrite: $\text{BiFeO}_3-(\text{Bi}_{0.5}\text{Na}_{0.25}\text{K}_{0.25})(\text{Ti}_{0.5}\text{Mn}_{0.5})\text{O}_3$ Ceramics

S. K. Sourav<sup>1</sup> · S. K. Parida<sup>2</sup> · R. N. P. Choudhary<sup>2</sup> · Umakant Prasad<sup>1</sup>

Received: 23 February 2023 / Revised: 30 June 2023 / Accepted: 14 July 2023 / Published online: 5 August 2023  
© The Korean Institute of Electrical and Electronic Material Engineers 2023

## Abstract

This communication describes a solid-state reaction prepared bismuth oxide and related complex compounds (BNKMT) of a chemical composition  $(1-x)\text{BiFeO}_3-x(\text{Bi}_{0.5}\text{Na}_{0.25}\text{K}_{0.25}\text{Ti}_{0.5}\text{Mn}_{0.5}\text{O}_3)$ , where  $x=0.15$  and  $0.20$ . Structural studies of the complex system show rhombohedral crystal symmetry (#R3c). The homogeneous distribution of the grains and grain boundaries throughout the sample surface clearly defined grain boundaries, which play a significant part in the conductivity mechanism, as revealed by the analysis of scanning electron microscopy micrographs and electrical properties. An energy-dispersive X-ray analysis spectrum was used to verify the processed materials' purity and composition. According to the analysis of the FTIR-ATR spectrum, the prepared samples show stretching bands that correspond to their constituent elements. A dielectric investigation confirmed that the Maxwell–Wanger type of dielectric dispersion is present in the samples. Studies of impedance parameters as a function of temperature and frequency result in a negative temperature coefficient of resistance behavior. While ac conductivity research supports the presence of a thermally activated relaxation process in the materials. Analysis of electric modulus discloses a non-Debye type relaxation mechanism in the studied sample. Because the samples are semiconducting at high temperatures, semi-circular arcs have been seen in both the Nyquist and Cole–Cole plots. When compared to BNKTM 15%, BNKTM 20% has a bandgap energy of 5.9 eV, according to the analysis of UV visible spectra.

**Keywords**  $(1-x)\text{BiFeO}_3-x(\text{BiNaKTiMnO}_3)$  · Rhombohedral · Maxwell–Wanger dielectric dispersion · Non-Debye relaxation · Thermally activated relaxation · Nyquist plots

## 1 Introduction

Since the discovery of ferroelectricity, numerous ferroelectric materials belonging to various structural families, such as perovskite, tungsten bronze, layer structure, etc., have been thoroughly researched. Among the members of the perovskite family, some substances such as potassium niobate ( $\text{KNbO}_3$ ), lead titanate ( $\text{PbTiO}_3$ ), lead zirconate ( $\text{Pb}(\text{Zr}, \text{Ti})\text{O}_3$ ), and barium titanate ( $\text{BaTiO}_3$ ) are frequently utilized for the capacitor, piezoelectric, and pyroelectric applications.

Due to the vast potential industrial applications of thin films of dielectric materials (in the form of ceramics (bulk and nano) with the correlations between their crystal structures and physical properties, these materials have extensively been researched [1–4]. Currently, a sizable group of material scientists is working to develop new ceramic materials for a variety of device applications, including actuators, IR detectors, gas sensors, modulators, multilayer capacitors, electro-optic, piezoelectric, computer memories, and display system devices, among others [5–9]. Nowadays, much attention is paid to the development of ferroic (multifunctional and multiferroic) materials for devices. The magnetic moment of Fe is ferromagnetic in (001) h/(111) c planes and anti-ferromagnetic in the two adjacent (001) h/(111) c planes in the structure of bulk  $\text{BiFeO}_3$ , which is a perovskite ferroic with G-type ordering [10]. Multiferroics are a subclass of functional materials that exhibit ferroelectric, ferromagnetic, and ferroelastic ordering characteristics all at the same time

✉ Umakant Prasad  
umakant.prasad@gmail.com

<sup>1</sup> Department of Physics, T.N.B. College, T.M. Bhagalpur University, Bhagalpur, Bihar 812007, India

<sup>2</sup> Department of Physics, ITER, Siksha O Anusandhan Deemed to be University, Bhubaneswar 751030, India

in a single phase [11]. As bismuth ferrite ( $\text{BiFeO}_3$ ) exhibits multiferroic properties at reasonable temperatures (much above room temperature), it has drawn particular interest among all multiferroic materials [12]. However, because of its high leakage current, structural distortion, and increased dielectric loss (tangent loss),  $\text{BiFeO}_3$  has been found to have some major problems in devices. These problems have an impact on the electrical and ferroelectric properties' strength, which restricts more on its multifunctional utility. The strong leakage current in  $\text{BiFeO}_3$  is attributed to iron ( $\text{Fe}^{2+} \rightarrow \text{Fe}^{3+} + e^-$ ) ion oxidation-reduction, which produces oxygen vacancies for charge compensation [13, 14]. It has also been discovered that pure bismuth-based compounds are one of the best candidates to replace the aforementioned deadly lead compounds. Such materials (Bi-based) have been chosen for particular devices based on their enhanced temperature stability, high ionic conductivity, low energy dissipation factor, high dielectric constant, and other factors.

Numerous studies on bismuth ferrite, single-dopant modified bismuth ferrite, and perovskite-doped bismuth have been published in the literature, but only very few have focused on complex perovskite ceramic BNKTM with  $(\text{Bi}_{0.5}\text{Na}_{0.25}\text{K}_{0.25})(\text{Ti}_{0.5}\text{Mn}_{0.5})\text{O}_3$  (modifier) and BFO (parent). It is noted that the same authors have investigated the structural, dielectric, electrical, and optical characteristics of above modified complex compounds with a chemical composition  $(1-x)\text{BiFeO}_3 - x(\text{Bi}_{0.5}\text{Na}_{0.25}\text{K}_{0.25})(\text{Ti}_{0.5}\text{Mn}_{0.5})\text{O}_3 = \text{BNKTM}$  ( $x=0.05$  and  $0.10$ ). They found that samples contain rhombohedral crystal structure (#R3c) for low concentration,  $x=0.05$  and  $0.10$  [15]. Now the authors are intended to synthesize (via ceramic technology) and study various properties (using standard characterization techniques) of the same compound with higher concentration ( $x=0.15$  and  $0.20$ ) in different experimental conditions to address several physical features and problems of the material.

## 2 Experimental Details

### 2.1 Material Required

The solid-state reaction method was used to prepare BNKTM of chemical composition  $(1-x)\text{BiFeO}_3 - x(\text{Bi}_{0.5}\text{Na}_{0.25}\text{K}_{0.25})(\text{Ti}_{0.5}\text{Mn}_{0.5})\text{O}_3$  ( $x=0.15$  and  $0.2$ ) ceramics. The starting raw materials (metal oxides and carbonate) are;  $\text{Bi}_2\text{O}_3$  (99.0%, Himedia),  $\text{Fe}_2\text{O}_3$  (99.5%, Himedia),  $\text{Na}_2\text{CO}_3$  (99.5%, Central Drug House),  $\text{K}_2\text{CO}_3$  (99.5%, Loba Chemie Pvt. Ltd),  $\text{TiO}_2$  (99.5%, Loba Chemie Pvt. Ltd) and  $\text{MnO}_2$  (99.5%, Loba Chemie Pvt. Ltd). The materials were weighted stoichiometrically with the

help of a digital balance (Model: ML204/A01) of accuracy up to the 4th decimal place. The required chemical equations to form the final product are given as; for  $x=15\%$  of dopant BNKTM:  $0.4625\text{Bi}_2\text{O}_3 + 0.425\text{Fe}_2\text{O}_3 + 0.01875\text{Na}_2\text{CO}_3 + 0.01875\text{K}_2\text{CO}_3 + 0.075\text{TiO}_2 + 0.075\text{MnO}_2 \rightarrow [0.85(\text{BiFeO}_3) - 0.15[(\text{Bi}_{0.5}\text{Na}_{0.25}\text{K}_{0.25})(\text{Ti}_{0.5}\text{Mn}_{0.5})\text{O}_3]] + 0.0375\text{CO}_2 \uparrow$  and similarly, for  $x=20\%$  of dopant BNKTM:  $0.45\text{Bi}_2\text{O}_3 + 0.40\text{Fe}_2\text{O}_3 + 0.025\text{Na}_2\text{CO}_3 + 0.025\text{K}_2\text{CO}_3 + 0.1\text{TiO}_2 + 0.1\text{MnO}_2 \rightarrow [0.80(\text{BiFeO}_3) - 0.20[(\text{Bi}_{0.5}\text{Na}_{0.25}\text{K}_{0.25})(\text{Ti}_{0.5}\text{Mn}_{0.5})\text{O}_3]] + 0.05\text{CO}_2 \uparrow$

### 2.2 Synthesis and Sintering

The mortar pestle was used to grind the metal powders for 2 h in a dry medium and then 2 h in a wet medium with the help of methanol. The fine powders were kept in a high-temperature resistant crucible in the furnace at  $800^\circ\text{C}$  for 10–12 h for calcination. The phase formation of the compounds was confirmed from the analysis of the X-ray diffraction (XRD) spectra of the calcined powders. The XRD spectra were obtained in a wide range of the Bragg angle, ( $20^\circ \leq 2\theta \leq 80^\circ$ ) using an X-ray diffractometer (Rigaku Ultima IV) with incident  $\text{Cu-K}_\alpha$  radiation ( $\lambda=1.5406 \text{ \AA}$ ). The cylindrical pellets of diameter 10–12 mm and thickness of 2 mm are made using nano-powders under a uniaxial hydraulic pressure of 4 MPa. For removal of impurity traces (C & O), better homogeneity dispersion, and high densification, the prepared pellets were sintered at  $850^\circ\text{C}$ .

### 2.3 Characterization

The structural analysis of the prepared samples was done by using the X-ray diffraction data (MODEL: RIGAKU Japan ULTIMA IV; equipped with a source of  $\text{CuK}_\alpha$  radiation ( $\lambda=1.5405 \text{ \AA}$ ). The study of the surface morphology and compositional analysis was done by using SEM-EDAX [MODEL: S-3400; SL. No. 340749-10]. The machine is working under the condition of accelerating voltage = 15,000 volts; working distance = 10,700  $\mu\text{m}$  and emission current = 113,000 nA. Both sides of the pellets were painted with high-conducting silver and heated at  $100^\circ\text{C}$  for 45 min before connecting to the two ends of the electrical electrode for evaluation of the electrical measurements. A phase-sensitive meter (N4L, model PSM-1735) was used for the measurement of dielectric and electrical properties, in a broad range of frequency (1000 Hz–1 MHz) and temperature ( $25^\circ\text{C}$ – $500^\circ\text{C}$ ). The UV–Vis spectra [MODEL: V-670, Sl. No.: A050461154, light source: D2/WI; Bandwidth: 2 nm] was used to obtain the required band gap within an absorbance range of 200–800 nm with a scan speed of 400 nm/min. The P–E loop tracer (M/S marine, India) was used to examine the possibility of ferroelectric property.

### 3 Results and Discussion

#### 3.1 XRD Analysis

Figure 1a, b shows XRD (X-ray diffraction) patterns of the  $(1-x)\text{BiFeO}_3 - x(\text{BiNaKTiMnO}_3)$ , ( $x=0.15$  and  $0.20$ ) ceramics. The Rietveld refinement of the proposed samples has been done using the CIF file-1001090 of  $\text{BiFeO}_3$  as reference taking computer program EXPO 2014 and the obtained fitting is shown in Fig. 1a BNKTM 15% and (b) BNKTM 20% respectively. The best possible structure was selected to be rhombohedral for both samples with a space group of  $R3c$  which is consistent with previous reports [15]. The reliability parameters extracted for BNKTM 15% from the refinement are  $R_{\text{wp}} (\%) = 5.286$  and  $R_p (\%) = 3.760$  with unit cell parameters  $a = b = 5.5689 \text{ \AA}$ ,  $c = 13.8130 \text{ \AA}$  and volume ( $V$ ) =  $371 \text{ \AA}^3$ .

Similarly, the reliability parameters extracted for BNKTM 20% from the refinement are  $R_{\text{wp}} (\%) = 6.519$  and  $R_p (\%) = 4.548$  with unit cell parameters  $a = b = 5.5761 \text{ \AA}$ ,  $c = 13.8201 \text{ \AA}$  and volume ( $V$ ) =  $372.14 \text{ \AA}^3$ . A small impurity phase is observed at  $27.8^\circ$ , which has no impact on other physical properties. As the XRD pattern of modified bismuth ferrite (BNKTM) (previously published [15] and present work) with all the compositions ( $x=0.05, 0.1, 0.15,$  and  $0.20$ ) looks similar, its structural parameters are concentration ( $x$ ) dependent.

Figure 1c, d represents Williamson–Hall plots of the BNKTM 15% and BNKTM 20% respectively. In the W–H plot,  $4 \sin\theta$  is taken along the x-axis and  $\beta \cos\theta$  is taken along the y-axis [16, 17]. The slope of the W–H plot provides lattice strain while the intercept will give the average crystallite size in the studied sample. The average crystallite size and lattice strain of the studied BNKTM 15% sample are found to be  $75.7 \text{ nm}$  and  $0.00349$  respectively. Similarly, the

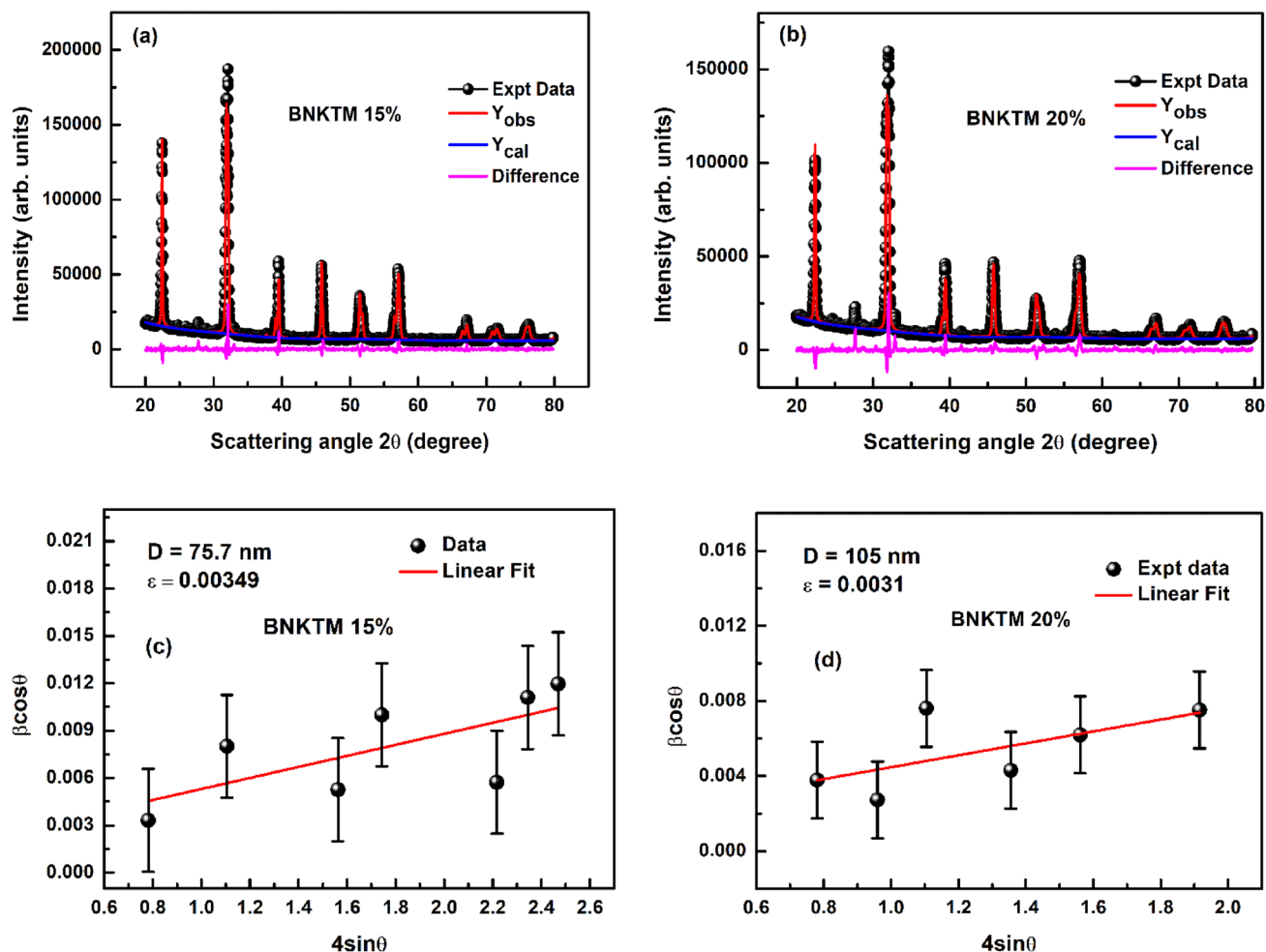


**Fig. 1** a XRD patterns of BNKTM 15% and b BNKTM 20% ceramics. c Williamson–Hall plots of BNKTM 15% and d Williamson–Hall plots of BNKTM 20%

average crystallite size and lattice strain of the BNKTM 20% sample are found to be 105 nm and 0.00310 respectively.

### 3.2 SEM and EDAX Analysis

Figure 2a represents the SEM micrograph of BNKTM 15%. The analysis of the SEM suggests that grains are distinctly visible and uniformly distributed over the surface of the sample with negligible voids. The grains are separated with well-defined grain boundaries; which may affect the electrical conduction mechanism. The purity and compositional analysis of the sample are shown in Fig. 2b. The EDAX spectrum confirms the presence of all constituent elements (Bi, Fe, Na, K, Ti, Mn & O) with both weight and atomic percentages. The distribution of grains of the BNKTM 15% surface is shown in Fig. 2c.

The average grain size of the sample was calculated using ImageJ software [18]. The value of the average grain is about 1.82  $\mu\text{m}$ . Similarly, Fig. 2d shows the SEM micrograph of the BNKTM 20%. The grains are well-grown and distributed uniformly on the whole surface of the sample with negligible voids. The grains are well-defined through the grain boundaries. The compositional analysis of the sample was done using an EDAX spectrum as shown in Fig. 2e. The results show the presence of signs of all the constituent elements (Bi, Fe, Na, K, Ti, Mn & O) in both weight and atomic percentage in the studied sample. Figure 2f shows the distribution pattern of the grains in the BNKTM 20%. The average grain size was calculated using ImageJ software and the result shows that the sample has an average grain of 1.71  $\mu\text{m}$ .

### 3.3 Dielectric Analysis

When an alternating electric field is applied across the dielectric materials, all types of polarizations are set up which may contribute to the relative permittivity/dielectric constant. Figure 3a, b shows the variation of the dielectric constant versus frequency of the BNKTM 15% and BNKTM 20% at some selected temperatures. At low frequencies, a wide dispersion in dielectric constant was observed due to the presence of all four types of polarization. This nature of the curve is called the Maxwell–Wanger type of dispersion. With the increase in the frequency of the applied electric field, the dielectric constant decreases and merged into one because of the reduction of the space charge polarization [19]. In this present study, the dielectric constant is maximum (i.e., 34,000) at  $x=0.15$  and then increases to 44,000 at  $x=0.20$  (at 50 °C and 1 kHz) This may be related to the suppression of the polarization effect at low frequency.

Figure 3c, d shows the variation of dielectric constant versus temperature at some selected frequencies for BNKTM 15% and BNKTM 20%. It is observed that the dielectric

constant approaches zero at low temperatures and then increases sharply. It is difficult to align all-electric dipoles in one direction at low temperatures; which gives a small dielectric constant. As soon as temperature increases, dipoles are aligned into a single direction and produce a high value of the dielectric constant [20]. In this present study, the highest value of the dielectric constant of 1650 is observed in BNKTM at 15% whereas the highest value of the dielectric constant of 36,000 is observed in BNKTM at 20%. The increasing trend may be related to the effect of composition in the prepared sample.

The effect of the frequency and temperature on dielectric loss is discussed in this section. Figure 4a–d shows the variation of the  $\tan\delta$  of the  $(1-x)\text{BiFeO}_3-x(\text{BiNaKTiMnO}_3)$  ( $x=0.15$  and  $0.20$ ) ceramics as a function of frequency ( $10^3$ – $10^6$  Hz) at a selected temperature of (25–500 °C). In this present study (Fig. 4a, b, the highest value of the dielectric loss is about 64 in BNKTM 15% whereas the highest value of the dielectric loss is about 48 in BNKTM 20%. Therefore, it may be concluded that BNKTM 20% is a better compound as compared to BNKTM 15% for application in energy storage devices and again well supported by dielectric results. Figure 4c, d shows the relation between the dissipation factor with the temperature. The result shows that the value of  $\tan\delta$  is very small and remains constant at low temperatures. Electric dipoles are not getting sufficient energy to be polarized in one direction at low temperatures, resulting smaller value of dielectric loss [21]. With the increase in temperature, dipoles start getting polarized and get maximum value. A sharp fall of dielectric loss curves around 350 °C was observed in BNKTM 15%, which may be related to phase transition i.e., ferroelectric to paraelectric phase. Similarly, a sharp fall of the dielectric loss curves at 300 °C may be related to the phase transition. Therefore, it may be concluded that the BNKTM 5% is more suitable to work for microelectronic devices both at high frequency and temperature.

### 3.4 Impedance Spectral Analysis

The role of impedance to control the electrical properties of the sample is discussed in this section. The complex impedance of a ceramic compound is described by the relation.  $Z^*(\omega) = Z'(\omega) + j Z''(\omega)$ , where  $Z'$  and  $Z''$  are the real and imaginary parts of the impedance and  $\omega$  is the angular frequency of the applied alternating field. The real and imaginary parts of the impedance are given by  $Z' = Z^* \cos\theta$  and  $Z'' = Z^* \sin\theta$  respectively [22]. Figure 5a, b shows the variation of real parts of the impedance of the BNKTM 15% and BNKTM 20% at some selected temperatures. The real part of the impedance decreases with the increase in temperature supporting the negative temperature coefficient of resistance behavior [23, 24]. The decreasing trend of the BNKTM 20%

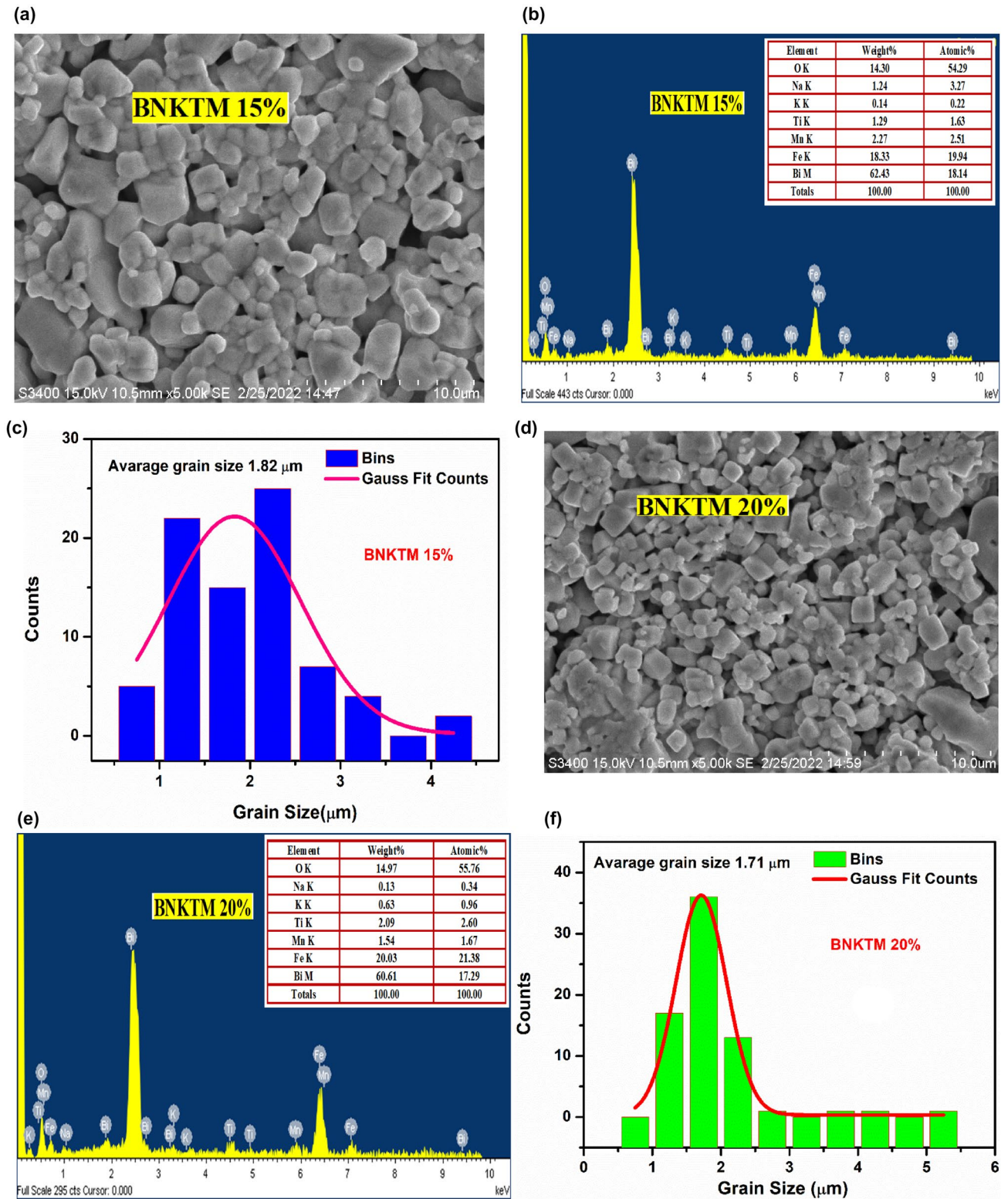


**Fig. 2** a Shows the SEM micrograph of BNKTM 15%; b EDAX spectrum; c distribution of grain size; d SEM micrograph of BNKTM 20%; e EDAX spectrum and f distribution of grains in BNKTM 20%

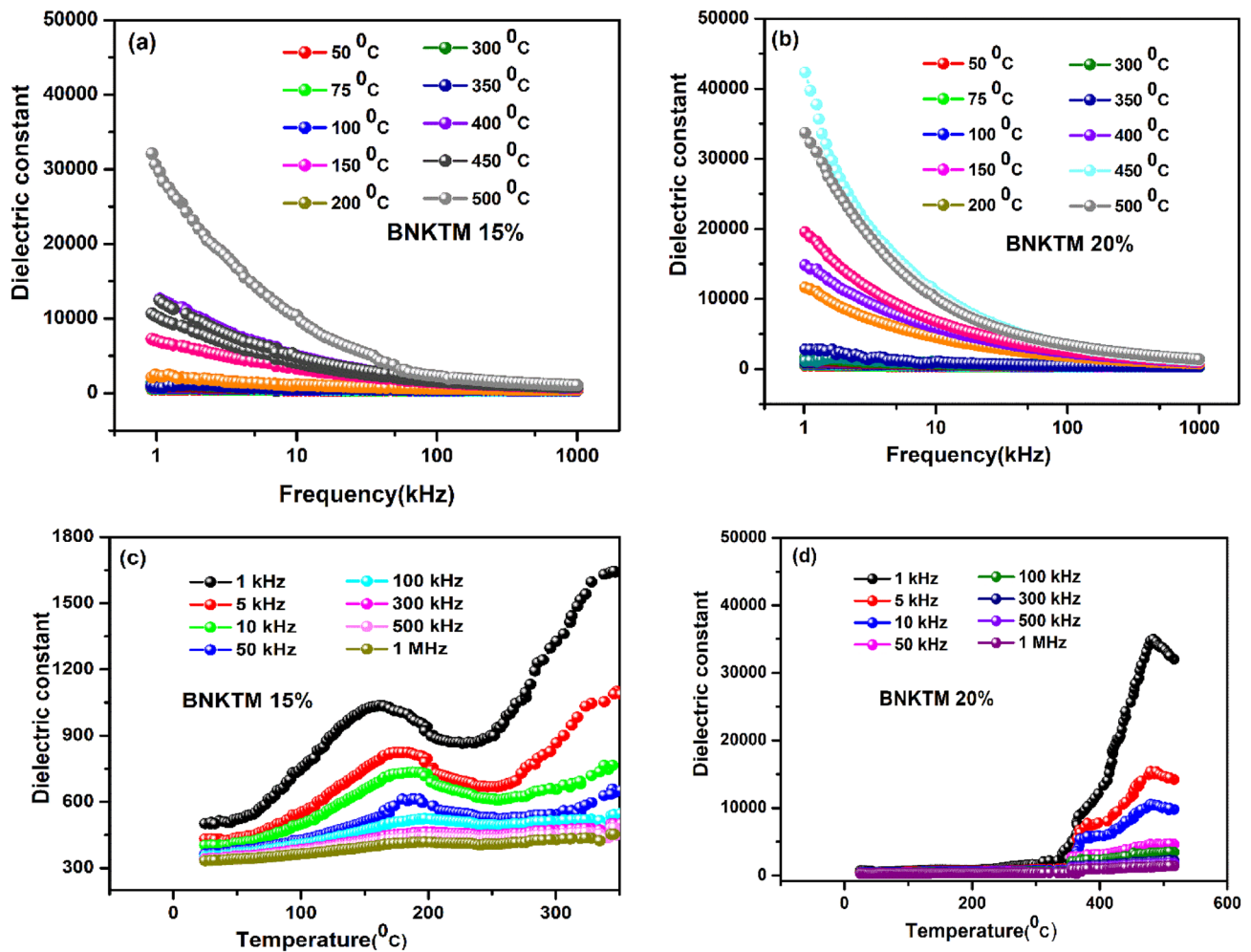


**Fig. 3** Plot dielectric constant versus frequency for **a** BNKTM 15%; **b** for BNKTM 20%; and plot between dielectric constant versus temperature **c** for BNKTM 15% and **d** for BNKTM 20%

is much sharper compared to BNKTM 15%. So, BNKTM 20% shows better NTCR behavior.

Figure 6a, b shows the variation of the imaginary part of the impedance of the BNKTM 15% and BNKTM 20% at some selected temperatures. The imaginary part of the impedance shows a wide disperse value at low frequency. Each plot has a peak value at a certain frequency called relaxation frequency. Therefore, the sample has a relaxation character which is useful for sensor applications. In close observation, the relaxation character of the BNKTM 20% is better than BNKTM 15%.

### 3.5 Nyquist and Cole–Cole Plots

Figure 7a, b represents the Nyquist plots for BNKTM 15% and BNKTM 20% at some selected temperatures. The formation of semi-circular arcs in the Nyquist plots confirms the semiconductor behavior [25]. Again, in the comparison,

the BNKTM 20% ceramic is having better semiconducting properties as compared to that of BNKTM 15%.

The semiconducting character of the sample was tested by using Cole–Cole plots as shown in Fig. 8a, b. The depressed semi-circular arcs present in the Cole–Cole plots confirm the semiconductor behavior; which is well-matched with Nyquist's results [26].

### 3.6 Modulus Analysis

The modulus analysis mechanism is widely used to study the space charge relaxation phenomena and ionic conductivity in ceramic material. Figure 9a, b represents the variation of the  $M'$  and  $M''$  with the frequency of BNKTM 15% and BNKTM 20% at some selected temperatures. The frequency-dependent electric modulus  $M'$  (real) and  $M''$  (imaginary) of  $(1-x)\text{BiFeO}_3-x(\text{BiNaKTiMnO}_3)$  have been shown at some selected temperatures. It is observed that all the values

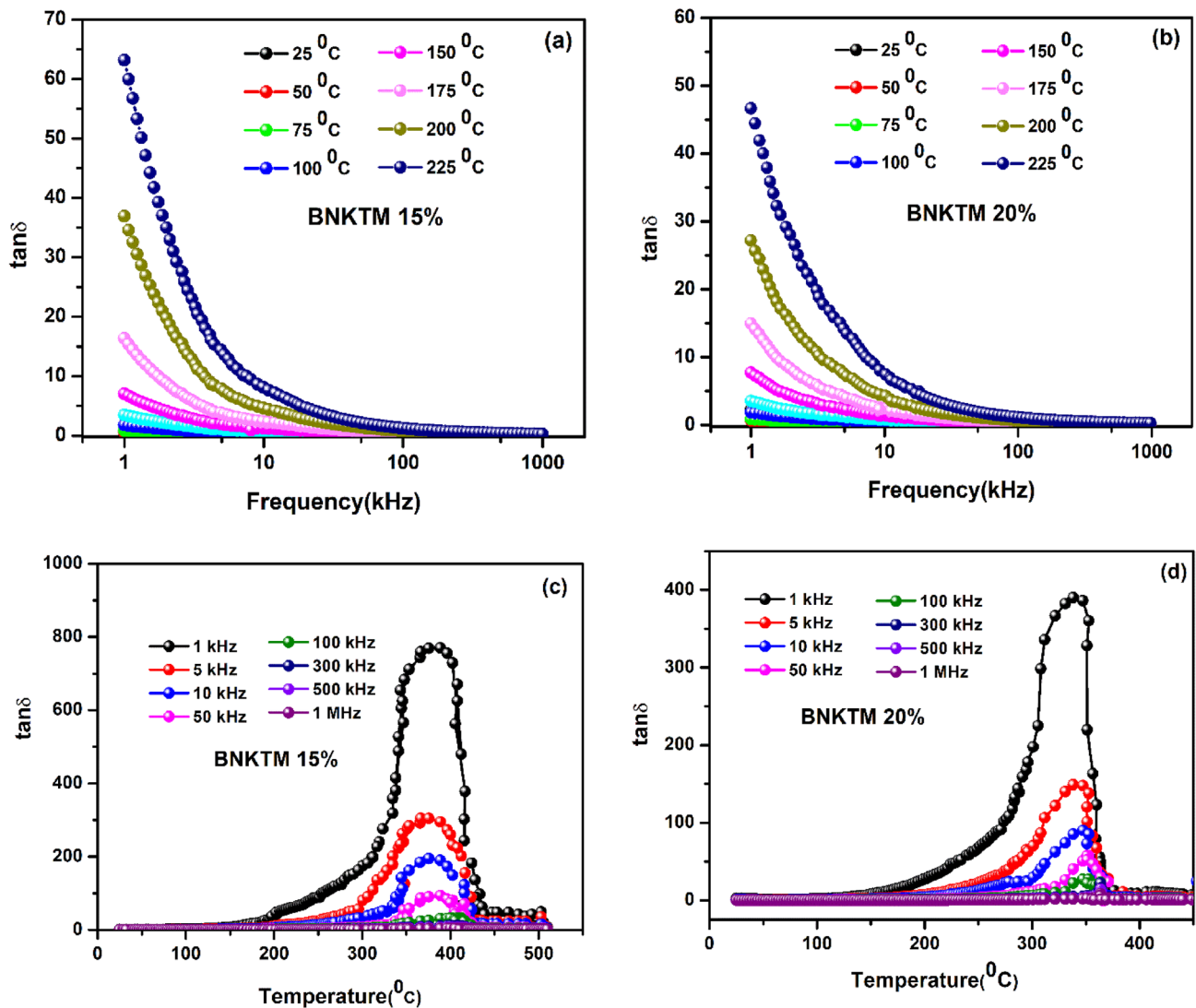


**Fig. 4** Plot between dielectric loss versus frequency for **a** BNKTM 15%; **b** BNKTM 20%; and plot between dielectric loss versus temperature for **c** BNKTM 15% and **d** BNKTM 20%

of  $M'$  are close to zero at low frequency and slowly increase with the rise in both frequency and temperature. The trend of the  $M'$  curves in BNKTM 20% has a better variation rate and is saturated at a high value compared to BNKTM 15%.

Figure 10a, b shows the variation of the  $M''$  with the frequency of the BNKTM 15% and BNKTM 20% at some selected temperatures. It is observed that the peaks of the  $M''$  are shifting with both frequency and temperature. The  $M''_{\max}$  peaks are shifted to the higher frequency side. This asymmetric peak shift confirms the presence of the non-Debye type of the relaxation process [27, 28]. The nature of dielectric relaxation shows the hopping mechanism of

the charge carrier dominantly at high temperatures. The asymmetric peaks are more pronounced in BNKTM 20% as compared to that BNKTM 15%. So, BNKTM 20% has a better non-Debye relaxation process.

### 3.7 AC Conductivity

Dielectric materials possess no free-charge carriers and are non-conducting in nature. Thus, when a solid polycrystalline dielectric material (ceramic pellet) is subjected to an external electric field, conduction takes place due to the transport of only weakly bound charged particles through different

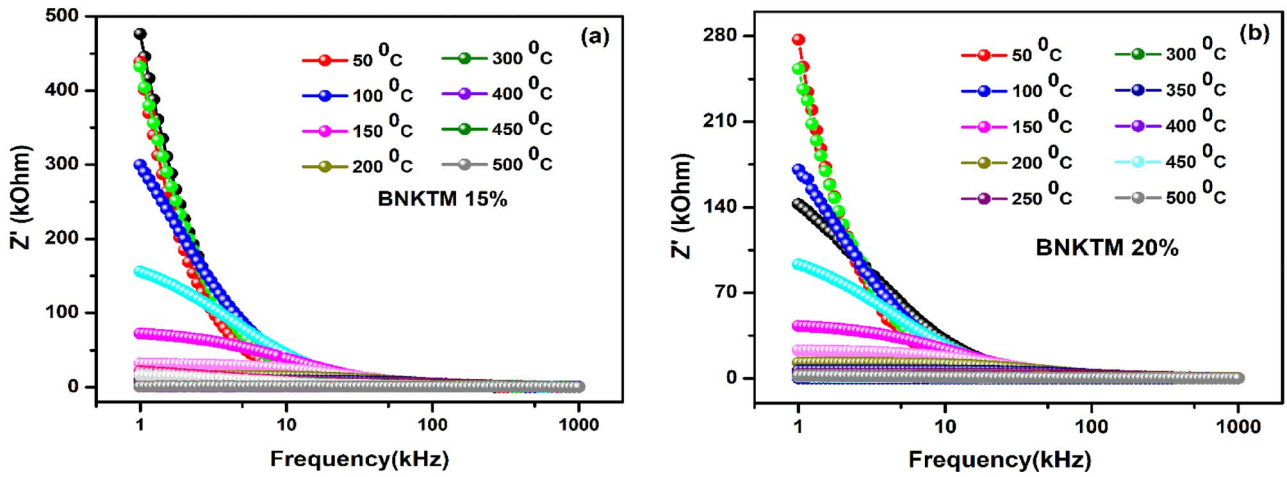


Fig. 5 Plots between  $Z'$  versus frequency for **a** BNKTM 15% and **b** BNKTM 20%

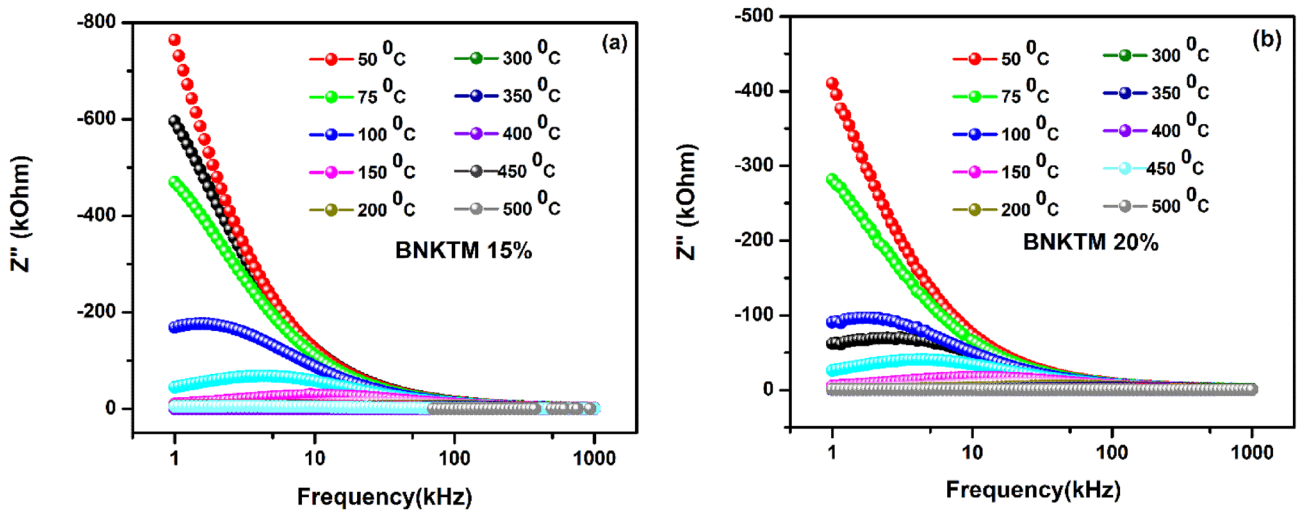


Fig. 6 Graph between  $Z''$  versus frequency for **a** BNKTM 15% and **b** BNKTM 20%

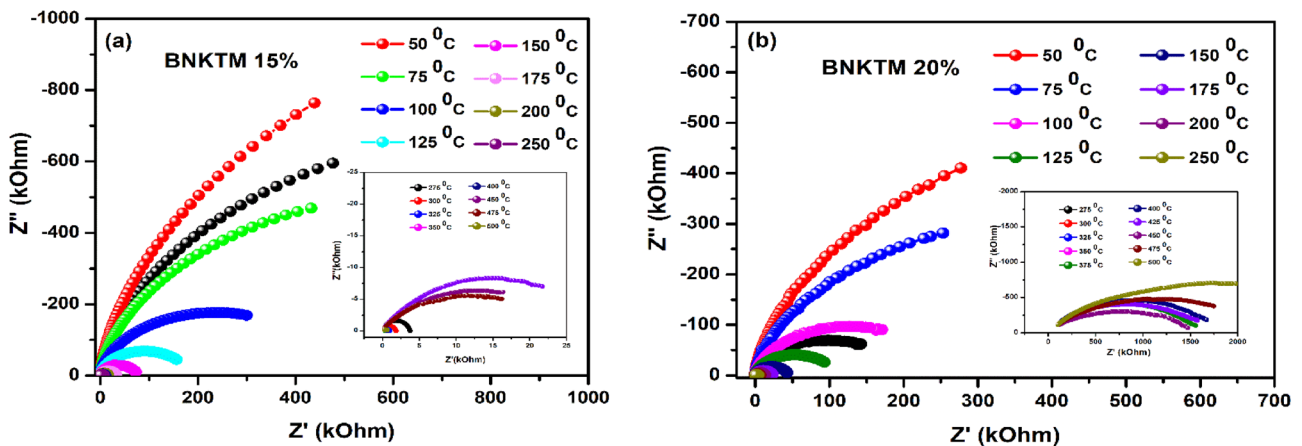


Fig. 7 Nyquist graph for **a** BNKTM 15% and **b** BNKTM 20% ceramics



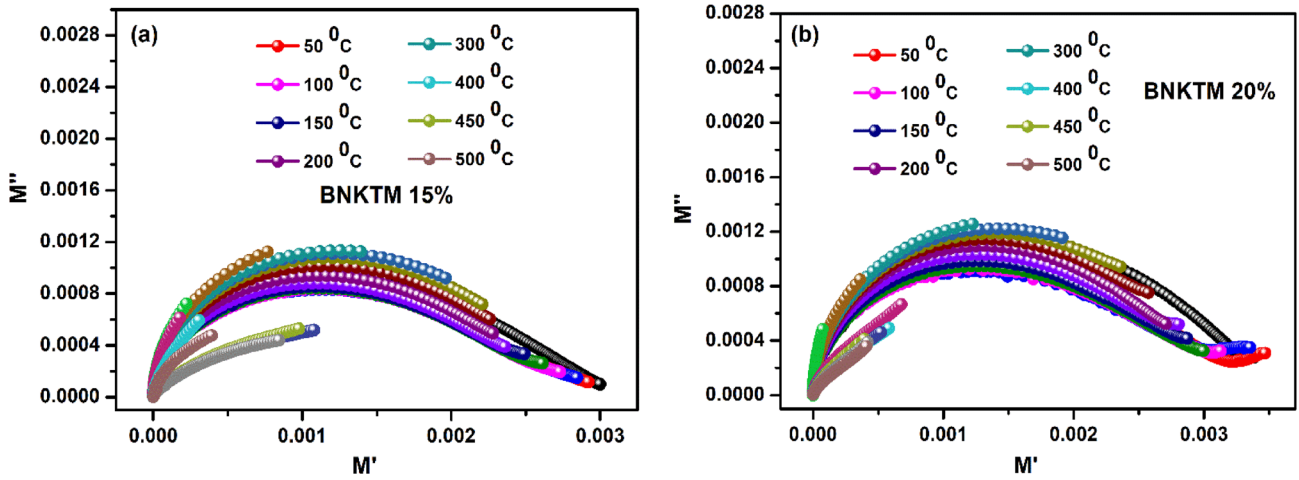


Fig. 8 Cole–Cole plots of a BNKTM 15% and b BNKTM 20% ceramics

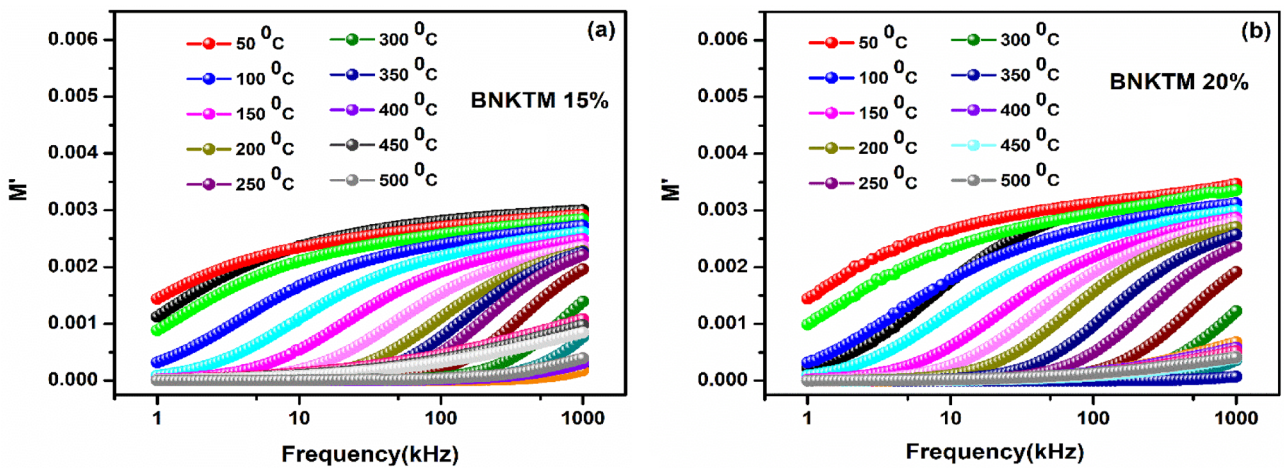


Fig. 9 Graph between  $M'$  and frequency for a BNKTM 15% b BNKTM 20%

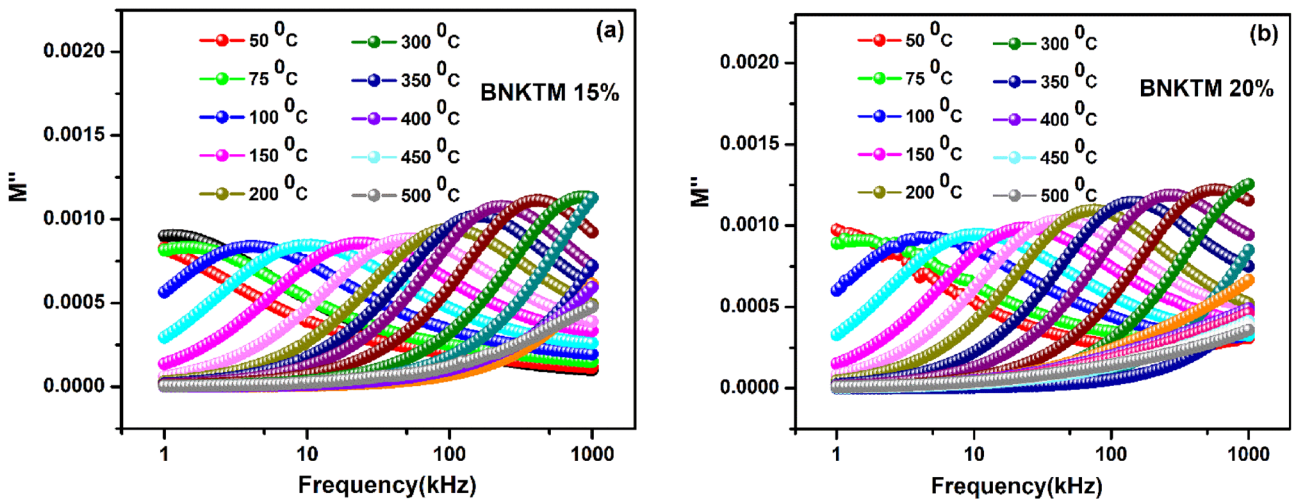


Fig. 10 Plot of  $M''$  versus frequency for a BNKTM 15% b BNKTM 20% ceramics

mechanisms. The conductivity can be calculated by using a relation;  $\sigma_{ac} = \omega \epsilon_r \epsilon_o \omega \tan\delta$ , where  $\omega$  is the angular frequency of the ac source,  $\tan\delta$  is the dielectric loss and  $\epsilon_o$  is the dielectric permittivity in vacuum), and the ac conductivity of the sample has been calculated [29]. Analysis of the ac conductivity of both samples BNKTM 15% and BNKTM 20% indicates that the conduction process follows Jonscher’s universal power law.

Figure 11a, b represents the variation of the ac conductivity with frequency for BNKTM 15% and BNKTM 20%. It is observed that the value of ac conductivity increases with the rise of frequency and is then merged into one. Again, the value of the ac conductivity is smallest at low frequency for 50 °C and then increases with the rise of the temperature. Figure 11c, d shows the variation of AC conductivity ( $\sigma_{ac}$ ) with the inverse of absolute temperature ( $10^3/T$ ) at different frequencies. The activation energy of the conduction process in the sample corresponding to the frequency can be

calculated by using the Arrhenius equation:  $\sigma_{ac} = \sigma_0 e^{-E_a/kT}$ , where  $\sigma_{ac}$  stands for ac conductivity,  $\sigma_0$  is the pre-exponential factor,  $k$  is the Boltzmann constant,  $T$  is the working temperature and  $E_a$  is the activation energy of the process [30]. The calculated activation energies for BNKTM 15% are; 143.82 meV, 138.67 meV, 135.50 meV, 125.14 meV, 119.29 meV, 108.84 meV, 103.50 meV and 96.6 meV at 1 kHz, 5 kHz, 10 kHz, 50 kHz, 100 kHz, 300 kHz, 500 kHz, and 1 MHz respectively. Similarly, the calculated activation energy for BNKTM 20% are; 143.71 meV, 141.39 meV, 135.43 meV, 125.25 meV, 118.58 meV, 107.87 meV, 101.93 meV, 93.63 meV at 1 kHz, 5 kHz, 10 kHz, 50 kHz, 100 kHz, 300 kHz, 500 kHz, and 1 MHz respectively. Analysis of both cases supports the presence of a thermally activated relaxation process in the sample. Again, when the activation energies for both samples are compared, it is observed

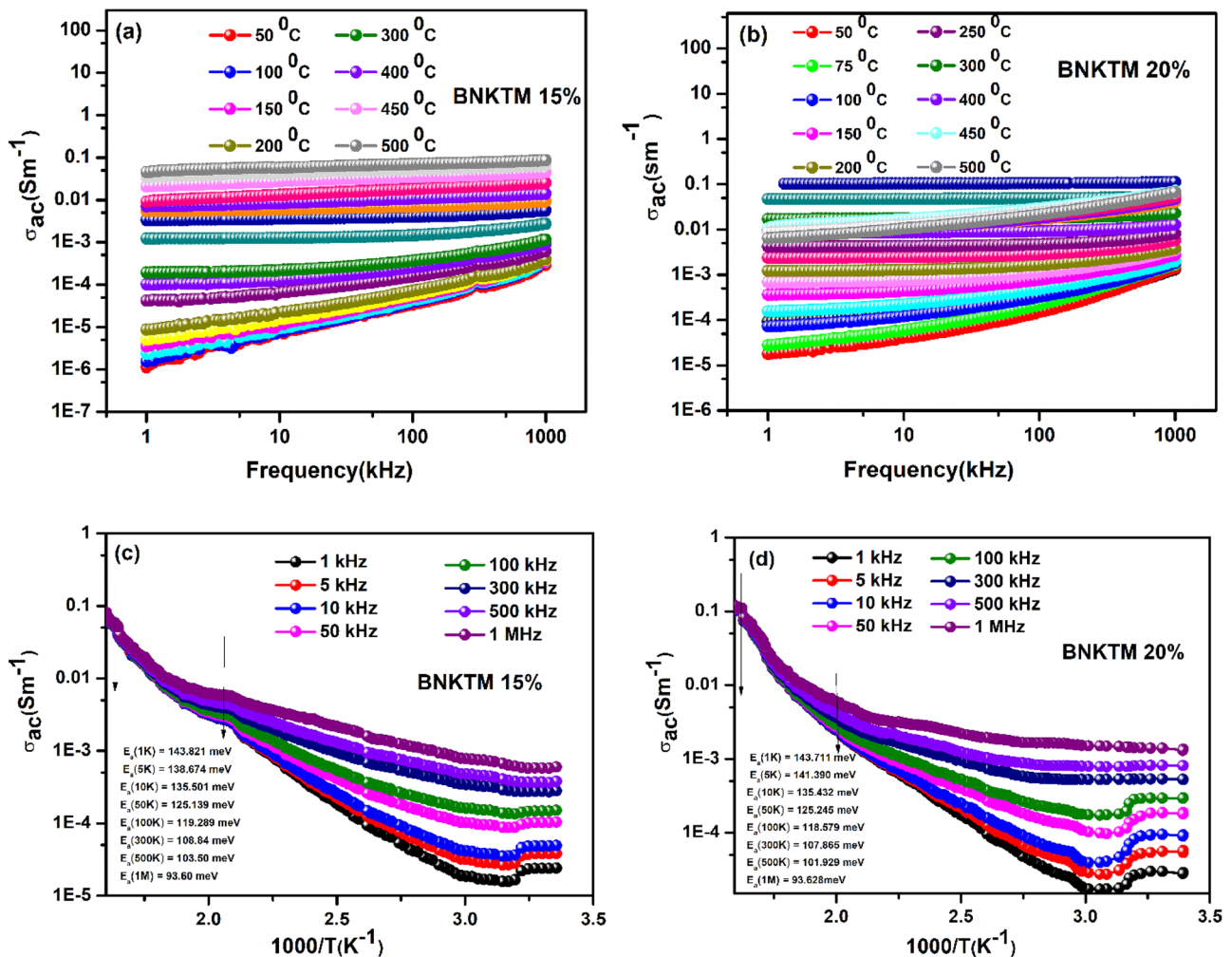


Fig. 11 Plot between ac conductivity versus frequency for a BNKTM 15%; b BNKTM 20%; and graph between ac conductivity versus temperature for c BNKTM 15% and d BNKTM 20%

that activation energy decreases with the rise of the dopant concentration.

### 3.8 UV Visible Spectroscopy

Absorbance spectra tailored in the respective optical study of the polycrystalline  $(1-x)\text{BiFeO}_3 - x(\text{BiNaKTiMnO}_3)$ , ( $x=0.15$  and  $0.20$ ) ceramics in the wider wavelength between the ranges of 200–1100 nm. The sharply falling region has been drawing attention to determining the band gap energy ( $E_{\text{gap}}$ ).

Tauc's relation has been used to resemble the semiconducting properties of the prepared sample. This relation provides the energy dependence absorption coefficient related by the following equation;  $\alpha = A(h\nu - E_{\text{gap}})^m/h\nu$  or  $(\alpha h\nu)^{1/m} = A(h\nu - E_{\text{gap}})$ , where  $A$  is known to be a constant whose value varies depending upon the type of transitions [31]. The value of  $m$  being an exponent is usually determined by the nature of electronic transitions involved during absorptions. The allowed direct, allowed indirect, forbidden direct, and forbidden indirect transitions can be obtained for the chosen values of  $m = 1/2, 2, 3/2,$  and  $3$  could be well defined.  $E_{\text{gap}}$  is called Tauc's optical bandgap while  $h\nu$  energy of the incident photon. Figure 12 a shows the absorbance spectrum [inset], 12 b shows the energy versus  $(\alpha h\nu)^2$  of the BNKTM 15% while 12 c shows the absorbance spectrum [inset] and 12 d shows the energy versus  $(\alpha h\nu)^2$  of the BNKTM 20% ceramics. The straight line extrapolated from the curve formed between  $(\alpha h\nu)^2$  versus  $h\nu$  yields the band gap energy depicted in Fig. 12. The calculated values of the energy band gap are about 5.8 eV and 5.9 eV for BNKTM

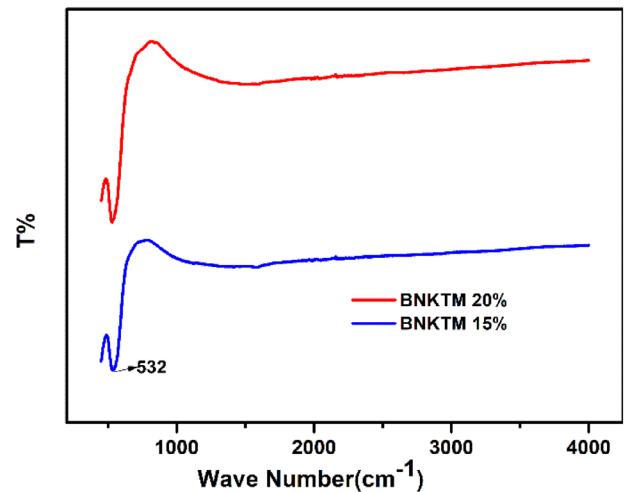


Fig. 13 FTIR-ATR spectrum of BNKTM 15% and BNKTM 20%

15% and BNKTM 20% respectively; which are a good range of energy for different optoelectronic device applications.

### 3.9 FTIR Study

Figure 13 shows the FTIR-ATR spectrum of the BNKTM 15% and BNKTM 20% within the wave number range of  $300\text{ cm}^{-1} \leq \tilde{\nu} \leq 4000\text{ cm}^{-1}$  which has been recorded using KBr-based reference material. The stretching band at  $532\text{ cm}^{-1}$  is due to the presence of all constituent elements in the prepared sample. The bandwidth decreases with an increased percentage of BNKTM in the host BFO ceramics.

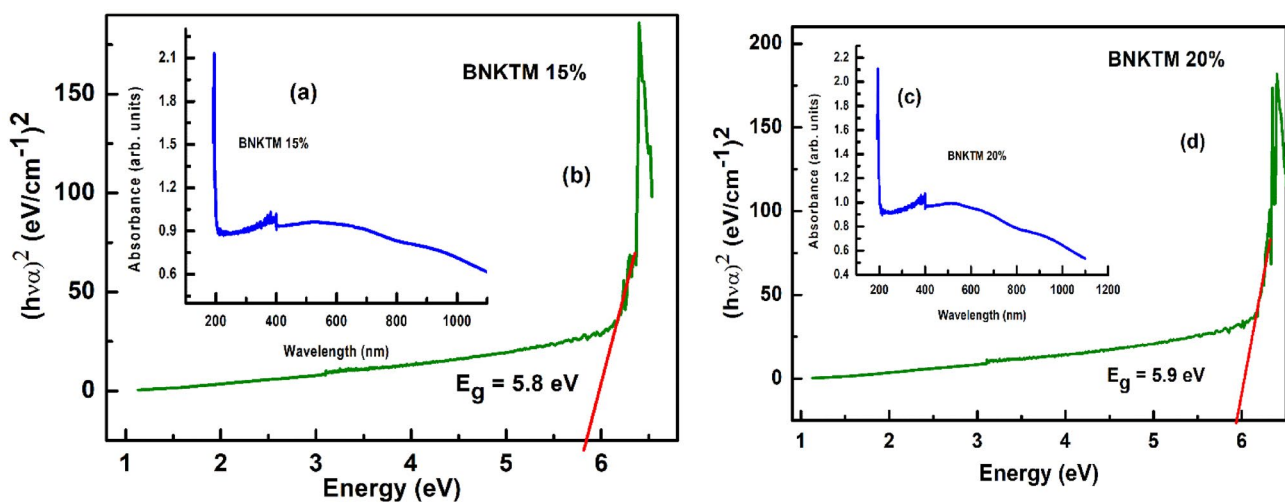


Fig. 12 a Absorbance versus wavelength (inset), b energy versus  $(\alpha h\nu)^2$  for BNKTM 15%, c absorbance versus wavelength (inset), and d energy versus  $(\alpha h\nu)^2$  for BNKTM 20% ceramic

## 4 Conclusions

Rhombohedral  $(1-x)\text{BiFeO}_3-x(\text{BiNaKTiMnO}_3)$ , ( $x=0.15$  and  $0.20$ ) ceramics were synthesized using a conventional solid-state reaction method. The XRD analysis confirms the formation of stable perovskites with average crystallite size and micro-lattice strain for  $x=0.15$  and  $0.20$  samples are found to be  $75.7\text{ nm}$ ,  $105\text{ nm}$ ,  $0.00365$ , and  $0.00310$  respectively. The study of SEM micrographs provides evidence of the uniform distribution of well-grown grains through distinct grain boundaries. The analysis of the EDAX spectrum reveals the true signature of all constituent elements (Bi, Fe, Na, K, Ti, Mn and O) in both weight and atomic percentage. The presence of the Maxwell–Wagner type of dielectric dispersion was confirmed by a dielectric study. The study of impedance as a function of temperature and frequency suggests a negative temperature coefficient of resistance (NTCR) behavior. The study of electric modulus reveals a non-Debye type of relaxation mechanism whereas the study of ac conductivity confirms a thermally activated relaxation process. Both Nyquist and Cole–Cole plots are showing semi-circular arcs; which is related to the semiconducting character of the sample.

**Acknowledgements** The authors would like to extend their gratitude and sincere thanks to Siksha O Anusandhan (Deemed to be University), Bhubaneswar for providing experimental facilities. We would like to thank Bandana, Preeti, and Sagarika for their support and encouragement.

## Declarations

**Conflict of interest** All authors declare that there is no conflict of interest.

## References

- J.R. Teague, R. Gerson, W.J. James, Dielectric hysteresis in single crystal  $\text{BiFeO}_3$ . *Solid State Commun.* **8**, 1073–1074 (1970)
- Z. Wang, C. Yuan, B. Zhu, Q. Feng, F. Liu, J. Xu, C. Zhou, G. Chen, Complex impedance spectroscopy of perovskite microwave dielectric ceramics with high dielectric constant. *J. Am. Ceram. Soc.* **102**, 1852–1865 (2019)
- R. Meher, R. Padhee, S.K. Parida, *Synthesis and Characterization of the  $(\text{BiFeO}_3)_{0.5}-(\text{CaTiO}_3)_{0.5}$  Solid Solution for some Device Applications*, vol. 12 (SPIN, 2022), pp. 2250023–2250011
- S.K. Parida, Studies on structural, dielectric, and optical properties of the lanthanum modified BF-BNT perovskite for the thermistor and photovoltaic applications. *Trans. Electr. Electron. Mater.* **23**, 632–641 (2022)
- C. Karthik, K.B.R. Varma, Dielectric and AC conductivity behavior of  $\text{BaBi}_2\text{Nb}_2\text{O}_9$  ceramics. *J. Phys. Chem. Solids.* **67**, 2437–2441 (2006)
- C. Miranda, M.E.V. Costa, M. Avdeen, A.L. Kholkin, J.L. Baptista, Relaxor properties of Ba-based layered perovskites. *J. Eur. Ceram. Soc.* **21**, 1303–1306 (2001)
- B. Harihara Venkataraman, K.B.R. Varma, Impedance and dielectric studies of ferroelectric  $\text{SrBi}_2\text{Nb}_2\text{O}_9$  ceramics. *J. Phys. Chem. Solids* **64**, 2105–2112 (2003)
- S. Lokovlev, C.H. Solter, M. Kuhnke, M. Es-Souni, Multiferroic  $\text{BiFeO}_3$  thin films processed via chemical solution deposition: structural and electrical characterization. *J. Appl. Phys.* **97**, 094901 (2005)
- R.N.P. Choudhary, D.K. Pradhan, G.E. Bonilla, R.S. Katiyar, Effect of La-substitution on structural and dielectric properties of  $\text{Bi}(\text{Sc}_{1/2}\text{Fe}_{1/2})\text{O}_3$  ceramics. *J. Alloys Compd.* **437**, 220–224 (2007)
- T. Zhao, A. Scholl, F. Zavaliche et al., Electrical control of antiferromagnetic domains in multiferroic  $\text{BiFeO}_3$  films at room temperature. *Nat. Mater.* **5**, 823–829 (2006)
- G. Catalan, J.F. Scott, Physics and applications of bismuth ferrite. *Adv. Mater.* **21**, 2463 (2009)
- J. Wang, J.B. Neaton, H. Zheng, V. Nagarajan, S.B. Ogale, B. Liu, D. Viehland, V. Vaithyanathan, D.G. Schlom, U.V. Waghmare, N.A. Spaldin, K.M. Rabe, M. Wuttig, R. Ramesh, Epitaxial  $\text{BiFeO}_3$  multiferroic thin film heterostructures. *Science* **299**, 1719 (2003)
- V.R. Palkar, J. John, R. Pinto, Observation of saturated polarization and dielectric anomaly in magnetoelectric  $\text{BiFeO}_3/\text{BiFeO}_3$  thin films. *Appl. Phys. Lett.* **80**, 1628 (2002)
- Y.P. Wang, L. Zhou, M.F. Zhang, X.Y. Chen, J.M. Liu, Z.G. Liu, Room-temperature saturated ferroelectric polarization in  $\text{BiFeO}_3/\text{BiFeO}_3$  ceramics synthesized by rapid liquid phase sintering. *Appl. Phys. Lett.* **84**, 1731–1733 (2004)
- S.K. Sourav, S.K. Parida, R.N.P. Choudhary, U. Prasad, Structural, microstructural, dielectric, transport, and optical properties of modified bismuth ferrite. *J. Korean Ceram. Soc.* (2022). <https://doi.org/10.1007/s43207-023-00294-5>
- S.K. Parida, Influence of cerium substitution on structural and dielectric properties of the modified  $\text{BiFeO}_3\text{-PbTiO}_3$  ceramics. *Ferroelectric.* **583**, 19–32 (2021)
- V.D. Mote, Y. Purushotham, B.N. Dole, Williamson–Hall analysis in estimation of lattice strain in nanometer-sized ZnO particle. *J. Theor. Appl. Phys.* **6**, 1–8 (2012)
- C.-T. Xia, V.M. Fuenzalida, R.A. Zarate, Electrochemical preparation of crystallized  $\text{Ba}_{1-x}\text{Sr}_x\text{MoO}_4$  solid-solution films at room temperature. *J. Alloys Compd.* **316**, 250–255 (2001)
- S.K. Parida, Studies on structural, dielectric, and optical properties of Cu/W double substituted calcium manganite for solar cells and thermistor applications. *Phase Trans.* **94**, 1033–1052 (2021)
- J. Liu, C.G. Duan, W.N. Mei, R.W. Smith, J.R. Hardy, Dielectric properties, and Maxwell–Wagner relaxation of compounds  $\text{ACu}_3\text{Ti}_4\text{O}_{12}$  ( $A = \text{Ca}, \text{Bi}_{2/3}, \text{Y}_{2/3}, \text{La}_{2/3}$ ). *J. Appl. Phys.* **98**, 1–6 (2005)
- M. Atif, M. Idrees, M. Nadeem, M. Siddique, M.W. Ashraf, Investigation on the structural, dielectric and impedance analysis of manganese substituted cobalt ferrite i.e.,  $\text{Co}_{1-x}\text{Mn}_x\text{Fe}_2\text{O}_4$  ( $0.0 \leq x \leq 0.4$ ). *RSC Adv.* **6**, 20876–20885 (2016)
- M. Lal, M. Chandrasekhar, R. Rai, P. Kumar, Structural, dielectric and impedance studies of KNNs–BKT ceramics. *Am. J. Mater. Sci.* **7**, 25–34 (2017)
- T. Moon, H.J. Lee, S.D. Hyun, B.S. Kim, C.S. Hwang, 2D electronics: origin of the threshold voltage shift in a transistor with a 2d electron gas channel at the  $\text{Al}_2\text{O}_3/\text{SrTiO}_3$  interface. *Adv. Electron. Mater.* **6**, 1900950 (2020)
- E.-D. Shin Kim, H.-J. Song, J. Hwang, Lee, S.-O. Yoon, P. Evolution, Thermal expansion, and microwave dielectric properties of cordierite- $\text{Al}_2\text{O}_3$  Composite. *J. Korean Inst. Electr. Electron. Mater. Eng.* **3**, 337–343 (2020)
- S.K. Parida, R.N.P. Choudhary, Preparation method and cerium dopant effects on the properties of  $\text{BaMnO}_3$  single perovskite. *Phase Trans.* **93**, 981–991 (2020)

26. S.K. Parida, P.K. Das, R.N.P. Choudhary, Structural and electrical characterization of  $\text{SrMn}_{0.97}\text{Ce}_{0.03}\text{O}_3$  ceramics. *Integr. Ferroelectr.* **221**, 215–230 (2021)
27. R. Ranjan, R. Kumar, N. Kumar, B. Behera, R.N.P. Choudhary, Impedance and electric modulus analysis of Sm-Modified  $\text{pb}(\text{Zr}_{0.55}\text{Ti}_{0.45})1x/4\text{O}_3$  ceramics. *J. Alloys Compd.* **509**, 6388–6394 (2011)
28. M. Hanief Najar, K. Majid, Investigation of the transport properties of PPy/[Co (EDTA) NH 3 c1] \$ H2O nanocomposite prepared by chemical oxidation method. *RSC Adv.* **6**, 25449–25459 (2016)
29. A.K. Pradhan, K. Zhang, D. Hunter, J.B. Dadson, G.B. Loiutts, P. Bhattacharya, R. Katiyar, J. Zhang, D.J. Sellmyer, U.N. Roy, Y. Cui, A. Burger, Magnetic and electrical properties of single-phase multiferroic  $\text{BiFeO}_3$ . *J. Appl. Phys.* **97**, 3–6 (2005)
30. S. Sahoo, P.K. Mahapatra, R.N.P. Choudhary, M.L. Nandagoswamy, Dielectric and impedance spectroscopy of (Ba, Sm) (Ti, Fe) $\text{O}_3$  system in the low-medium frequency range. *J. Mater. Sci. Mater. Electron.* **26**, 6572–6584 (2015)
31. N. Saha, A. Sarkar, A.B. Ghosh, A.K. Dutta, G.R. Bhadu, P. Paul, B. Adhikary, Highly active spherical amorphous  $\text{MoS}_2$ : facile synthesis and application in photocatalytic degradation of rose bengal dye and hydrogenation of nitroarenes. *RSC Adv.* **5**, 88848–88856 (2015)

**Publisher's Note** Springer Nature remains neutral with regard to jurisdictional claims in published maps and institutional affiliations.

Springer Nature or its licensor (e.g. a society or other partner) holds exclusive rights to this article under a publishing agreement with the author(s) or other rightsholder(s); author self-archiving of the accepted manuscript version of this article is solely governed by the terms of such publishing agreement and applicable law.